

Scalable Pulsed Laser Deposition of Transparent Rear Electrode for Perovskite Solar Cells

Yury Smirnov,* Laura Schmengler, Riemer Kuik, Pierre-Alexis Repecaud, Mehrdad Najafi, Dong Zhang, Mirjam Theelen, Erkan Aydin, Sjoerd Veenstra, Stefaan De Wolf, and Monica Morales-Masis*

Sputtered transparent conducting oxides (TCOs) are widely accepted transparent electrodes for several types of high-efficiency solar cells. However, the different sputtering yield of atoms makes stoichiometric transfer of target material challenging for multi-compounds. Additionally, the high kinetic energies of the arriving species may damage sensitive functional layers beneath. Conversely, pulsed laser deposition (PLD) is operated at higher deposition pressures promoting thermalization of particles. This leads to stoichiometric transfer and additionally reduces the kinetic energy of ablated species. Despite these advantages, PLD is rarely used within the photovoltaic community due to concerns about low deposition rates and the scalability of the technique. In this study, wafer-scale (4-inch) PLD of high-mobility Zr-doped In_2O_3 (IZrO) TCO for solar cells is demonstrated. IZrO films are grown at room temperature with deposition rate on par with RF-sputtering ($>4 \text{ nm min}^{-1}$). As-deposited IZrO films are mostly amorphous and exhibit excellent optoelectronic properties after solid phase crystallization at $<200 \text{ }^\circ\text{C}$. 100-nm thick films feature a sheet resistance of $21 \text{ } \Omega \square^{-1}$ with electron mobilities $\approx 70 \text{ cm}^2 \text{ V}^{-1} \text{ s}^{-1}$. PLD-grown IZrO is applied as rear electrode in efficient semi-transparent halide perovskite solar cells leading to the improved stabilized maximum power point efficiency (15.1%) as compared to the cells with sputtered ITO electrodes (11.9%).

1. Introduction

Pulsed laser deposition (PLD) is an established technique to deposit thin films with complex stoichiometry that has gained significant research attention after successful fabrication of high-temperature superconductors (HTS) in thin film form.^[1] Since then, PLD was mainly used for applications related to epitaxial growth of multi-compound oxides on lattice-matched substrates but has yet to be explored within the photovoltaic (PV) community. Although highly conductive In-based TCOs were fabricated by PLD and successfully implemented as front contact in OLEDs^[2,3] in early 2000s, there are still few reports regarding application of PLD-grown contacts in PV devices. Literature reports include doped ZnO films for CIGS^[4] and organic^[5] solar cells and metal oxide transport layers for halide perovskite solar cells.^[6] Moreover, PLD has been proposed for chalcogenide absorber fabrication^[7,8] and, more recently, for halide perovskite absorber layers.^[9,10]

Nevertheless, PLD is still considered to be an exotic fabrication method in the PV community due to the common concerns about the scalability of the technique reasoned by limited substrate size for uniform coating and low deposition rates. In fact, significant progress in upscaling^[11] has already allowed fabrication of high-quality piezoelectric devices on 200 mm circular wafers,^[12] as well as annual fabrication of $>100 \text{ km}$ of HTS tape with deposition rates $>750 \text{ nm min}^{-1}$ by PLD.^[13] Here we demonstrate scalable PLD for the fabrication of Zr-doped In_2O_3 (IZrO) thin films with properties on par with RF-sputtered ones. Furthermore, we apply IZrO films as rear electrodes in proof-of-concept semi-transparent halide perovskite solar cells.

2. Background of PLD Process

The principle of PLD processes is illustrated in **Figure 1a** and is briefly summarized below. The target, placed in a vacuum chamber with base pressure of $<10^{-7}$ mbar, is repeatedly ablated by the focused laser beam (typically, an excimer UV laser) with

Y. Smirnov, L. Schmengler, R. Kuik, Dr. P.-A. Repecaud, Prof. M. Morales-Masis
 MESA+ Institute for Nanotechnology
 University of Twente
 Enschede, AE 7500, Netherlands
 E-mail: y.smirnov@utwente.nl; m.moralesmasis@utwente.nl
 Dr. M. Najafi, Dr. D. Zhang, Dr. M. Theelen, Dr. S. Veenstra
 TNO/Solliance
 High Tech Campus 21, Eindhoven, AE 5656, Netherlands
 Dr. E. Aydin, Prof. S. De Wolf
 King Abdullah University of Science and Technology (KAUST)
 KAUST Solar Center (KSC)
 Physical Sciences and Engineering Division (PSE)
 Thuwal 23955-6900, Saudi Arabia

 The ORCID identification number(s) for the author(s) of this article can be found under <https://doi.org/10.1002/admt.202000856>.

© 2021 The Authors. Advanced Materials Technologies published by Wiley-VCH GmbH. This is an open access article under the terms of the Creative Commons Attribution License, which permits use, distribution and reproduction in any medium, provided the original work is properly cited.

DOI: 10.1002/admt.202000856

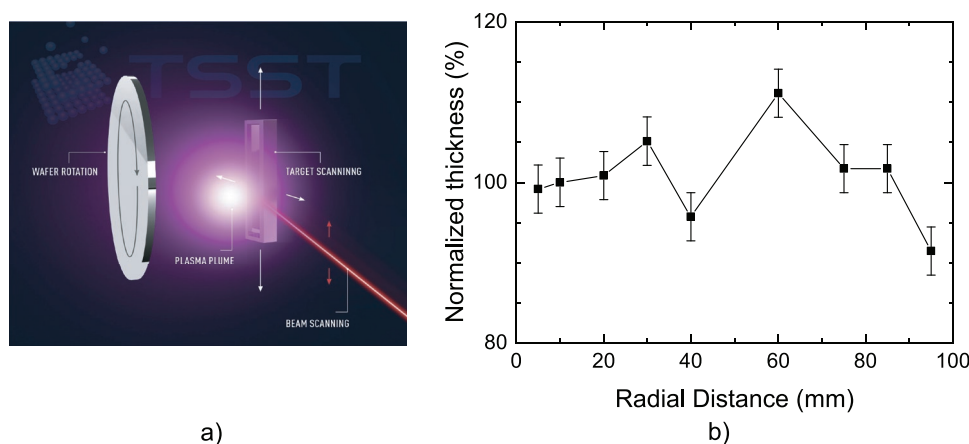


Figure 1. a) Illustration of the large area pulsed laser deposition process consisting of an excimer laser locally ablating a target creating a plasma plume. Target scanning and wafer rotation are the key features for uniform wafer coverage. Drawing courtesy of Twente Solid State Technology, Demcon group. b) Thickness profile obtained over 4-inch circular wafer.

pulses of ns duration. This leads to explosive removal of the material from the target surface confined in the plasma plume that expands in the direction perpendicular to the substrate. The ablation process typically takes place in the background gas environment which serves the purpose of thermalizing the energetic species, as well as providing additional supply of elements (e.g., oxygen for the deposition of oxides) to compensate for lack of stoichiometry. The plasma plume is significantly smaller than the 4-inch substrate leading to non-uniform thickness distribution when collected statically on substrates bigger than 1-inch. Therefore, the laser spot is scanned over the target to obtain homogeneous films on larger substrates. In addition to the plume spatially scanning over the 4-inch wafer in the lateral direction, the substrate holder is rotated to ensure a complete coverage of the plume over the full wafer.

The precise physics underlying the deposition process is more complex than sketched here and is thoroughly reviewed in references.^[14,15] Nevertheless, it is important to highlight the main advantages of PLD.

1. Allowing stoichiometric transfer of elements independent of their volatility and evaporation pressures.
2. Providing flexibility for processing parameters since the energy source for material ablation is physically decoupled from the vacuum equipment. This gives a larger choice for deposition pressures as no restriction for glow discharge pressure is present. This also allows control of particles' kinetic energy when landing on the substrate.
3. Allowing the precise control of the number of arriving particles enabling layer-by-layer growth thanks to the pulsed nature of the process.

Atomic layer engineering, mentioned in point 3, is greatly associated with in-situ growth monitoring with reflection high-energy electron diffraction (RHEED)^[16] allowing monolayer growth control. However, we do not further elaborate on this feature here, as it is less relevant for the growth of polycrystalline films discussed in this work. On the other hand, we discuss other above-mentioned advantages by comparing the properties of the PLD-grown and sputtered films of IZrO from the same target composition.

3. Experimental Section

3.1. Zr-Doped In₂O₃ Fabrication and Analysis

The IZrO films were grown on glass substrates at room temperature using a large area PLD system (Twente Solid State Technologies) with capabilities for deposition on up to 4-inch wafers. Glass substrates were ultrasonicated in acetone and isopropanol for 5 minutes and rinsed in deionized water prior to a deposition. A KrF excimer laser ($\lambda = 248$ nm) was used for all experiments with the repetition rate of 20 Hz and the fluence of 1.9 J cm^{-2} .

The total working pressure was 0.02 mbar with the optimized oxygen to total flow ratio $r(\text{O}_2) = \text{O}_2/(\text{Ar}+\text{O}_2)$ of 20%. It is important to mention that this working pressure is almost one order of magnitude higher than typically used in magnetron sputtering (0.0013 mbar as equivalent of 1 mTorr, for instance). This is expected to slow down the arriving species and enable “soft landing” on top of sensitive transport layers^[5,17,18] and as briefly discussed in Section 4.4.

Deposition rates for the complex oxide growth is commonly estimated in nm per pulse as certain amount of pulses corresponds to one monolayer of the deposited material and can be monitored by intensity oscillation of the RHEED pattern. This is not directly informative for the growth of polycrystalline IZrO as the same deposition rate per pulse would correspond to different thicknesses if the repetition rate is varied. Therefore, it is estimated that the deposition rate as the overall thickness divided by the deposition time. 2.5×10^4 pulses leads to ≈ 100 nm of the deposited IZrO film. This, assuming a commonly used repetition rate of 10 Hz, corresponds to the deposition rate of $\approx 2.5 \text{ nm min}^{-1}$. The deposition rate was further improved to $\approx 5 \text{ nm min}^{-1}$ increasing the repetition rate to 20 Hz without sacrificing the optoelectronic properties.

The uniformity of a typical PLD IZrO film (≈ 120 nm) across the horizontal axis on a 4-inch substrate is displayed in Figure 1b. The thickness of the surface step height on samples placed across the x -axis was measured by a stylus profilometer with the tolerance of $\pm 3\%$ of 120-nm film thickness due to the tip available. Normalized thickness was calculated as

the ratio between the thickness at the measured point and its mean value across the x -axis of the wafer. Overall, thickness uniformity of $\pm 5.3\%$ on the full wafer is obtained. Maximum variation of $\approx 10\%$ is observed in the center area (which can also be a single measurement outlier) and would be further addressed by optimizing the plume-scan curve. Moreover, solar cell precursors with 9 cm^2 area were placed closer to the 4-inch substrate edges as demonstrated in Section 4.4. The local thickness uniformity in this 30 mm region is $\pm 2.5\%$. Thicknesses of films were verified by X-ray reflectivity measurements as displayed in Figure S2, Supporting Information. Clearly visible interference fringes indicate highly smooth surfaces of IZrO layers given the large density contrast between glass and In_2O_3 . Fitting of the measured specular reflectivity scans demonstrate root mean squared surface roughness below 0.75 nm for all IZrO samples (PLD-grown and sputtered TCO films both in as-deposited and annealed state as would be elaborated below).

To study the evolution of the structural and optoelectronic properties of the IZrO films with temperature, as well as for full comparison with sputtered IZrO films, as-deposited IZrO electrodes were post-annealed at $200\text{ }^\circ\text{C}$ in air for 30 min. This temperature budget is not compatible for films deposited on top of the perovskite absorber layer. However, the enhanced optoelectronic performance after the heat treatment step (as shown in Section 4.1) is beneficial if IZrO film is applied as front electrode in four-terminal (4T) tandem devices or in silicon heterojunction cells with a thermal budget of $200\text{ }^\circ\text{C}$.^[19] Comparison of properties was done with IZrO films grown by RF-sputtering at KAUST following procedure described by Aydin et al.^[20] All films analyzed were deposited (both by PLD and sputtering) from a 98/2 wt% $\text{In}_2\text{O}_3/\text{ZrO}_2$ target. Microstructure of the films was inspected by grazing incidence X-ray diffraction (GI-XRD) with the incident angle (ω) = 0.6° . A heating stage was used for the in situ study of amorphous-to-polycrystalline transition. The electrical resistivity (ρ), carrier concentration (N_e), and Hall mobility (μ_{Hall}) were extracted from Hall effect measurements in the Van der Pauw configuration. The optical transmittance (T) and reflectance (R) of the films were measured by UV-vis-NIR spectrometer with an integrating sphere. Absorbance (A) was determined from $100 - T - R$.

3.2. Solar Cell Fabrication and Analysis

Semi-transparent perovskite solar cells (ST-PSC) were prepared inside the glovebox with N_2 environment and the oxygen and moisture levels at about 1 ppm. 9 cm^2 area Corning XG glass substrates were cleaned sequentially with soap, deionized water and isopropanol in an ultrasonic bath prior to the front electrode fabrication. Sn-doped In_2O_3 (ITO) was deposited at room temperature using an AJA RF magnetron sputtering system from a 90/10 wt% $\text{In}_2\text{O}_3/\text{SnO}_2$ target onto glass substrates for the front contact and on top of the perovskite cells for comparison of rear electrode performance. All ST-PSC cells reported have the same ITO front electrode. The ITO was deposited in Ar/O_2 atmosphere at the process pressure of 2 mTorr and oxygen to total flow ratio $r(\text{O}_2) = 0.23\%$. The RF power density was 0.7 W cm^{-2} . An $\approx 10\text{ nm}$ thick hole transport layer (HTL) made of poly(triarylamine), (PTAA) and an $\approx 500\text{ nm}$ thick

$\text{Cs}_{0.15}(\text{FA}_{0.85})\text{Pb}(\text{I}_{0.98}\text{Br}_{0.02})_3$ perovskite absorber layer (bandgap of 1.55 eV) were deposited by spin coating. Further details on fabrication of the perovskite precursor and HTL solutions are provided in Glowienka et al.^[21] Electron transport layers (ETLs) consisting of $\approx 20\text{ nm}$ of C_{60} and $\approx 8\text{ nm}$ of Bathocuproine (BCP) were subsequently deposited by thermal evaporation. The fabrication of ST-PSC was finished by rear TCO deposition at room temperature of either ITO ($\approx 180\text{ nm}$) by RF-sputtering at Solliance, or IZrO ($\approx 130\text{ nm}$) by PLD at University of Twente. The thickness of both TCOs was optimized to obtain a sheet resistance (R_{sh}) of $50\ \Omega\ \square^{-1}$. Reference opaque solar cells were finished with thermal evaporation of 100 nm Cu films as the rear electrode. In case of PLD depositions, samples were sealed in a glovebox environment during both sample exchanges (before and after TCO deposition). MgF_2 layers were thermally evaporated on glass to reduce reflection losses in the visible range.

ST-PSC were measured under AM1.5G spectrum in a glovebox from the glass side (superstrate configuration). A stainless steel mask was used to define the active area of 0.09 cm^2 . The light intensity was calibrated by a silicon reference cell. The J - V curves were measured using a Keithley 2400 at a scanning rate of 200 mV s^{-1} . The stabilized PCE was obtained by tracking the output power for 5 min.

4. Results and Discussion

4.1. Zr-Doped In_2O_3 : Optoelectronic Properties of PLD-Grown Films and Comparison with Films Grown by RF-Sputtering

Figure 2 displays the transmittance and absorbance curves as a function of wavelength for the 100-nm IZrO thin films grown by PLD and RF-sputtering before and after annealing. The films exhibit similar properties: low absorbance in the measured spectral range (300–1500 nm) for as-deposited state which further drops below 10% after the annealing step. Decreased absorbance in the near infrared (NIR) for the sputtered films, is caused by suppressed free carrier absorption (FCA) due to the decrease of N_e (Table 1) after the heat treatment. In contrast, PLD-grown films demonstrate negligible differences in NIR transmittance after annealing, which is also in-line with only a slight increase in free carrier density after annealing (Table 1). A common observation, for PLD and sputtered films, is the widening of the band gap after annealing. Previous reports suggest that this is linked to the phase transition from an amorphous to a polycrystalline state,^[22–24] as will be demonstrated in the next section. This structural transition also affects electrical properties of the films. For IZrO deposited by either, PLD or sputtering, the Hall mobility increases after the annealing step at $200\text{ }^\circ\text{C}$ reaching $>70\text{ cm}^2\text{ V}^{-1}\text{ s}^{-1}$ which is more than twice the as-deposited value.

While the increase in μ_e is consistent for films deposited with both methods, the N_e present different trends. Three possible dopants could influence N_e in IZrO films, namely: Zr^+ atoms, atomic hydrogen, and oxygen vacancies. The N_e of the as-deposited sputtered films is higher than the N_e of the as-deposited PLD films (6.2 vs. $4.7 \times 10^{20}\text{ cm}^{-3}$), which intuitively indicates that the sputtered films have a larger amount of oxygen vacancies or higher hydrogen content as compared to the PLD-grown

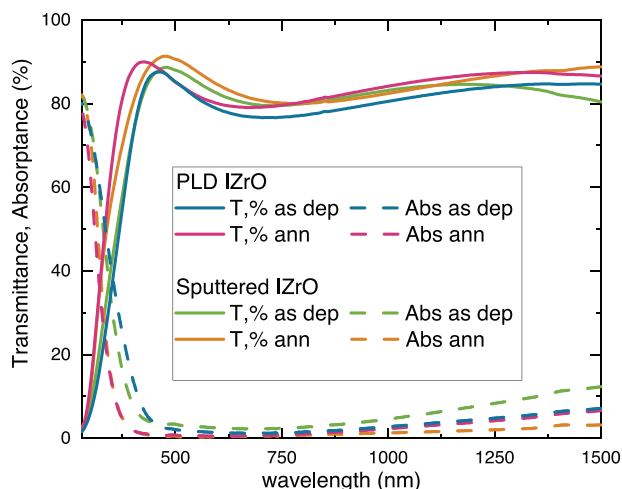


Figure 2. Transmittance (T) and absorbance (Abs) of IZrO films, as-deposited (RT) and annealed (200 °C in air) grown by PLD and RF-sputtering, respectively. The graph shows a band gap blue shift after annealing and an overall absorbance of less than 10% from the visible to the near infrared part of the spectrum.

films. The N_e of the sputtered IZrO drops considerably after the heat treatment, which has been previously explained by the uptake of oxygen by the films from the air.^[25,26] Another possible cause of decreased N_e , as described by Koida et al.,^[27] is hydrogen effusion or hydrogen passivation of oxygen vacancies during solid phase crystallization. Even though IZrO films are deposited without intentionally introducing water (like normally done for IO:H), H₂O will be present at a background pressure of 10⁻⁶ to 10⁻⁷ mbar. Contrary, the PLD films have lower carrier density as-deposited, hinting toward more oxidized conditions (and/or leaner hydrogen content) and therefore a competition of oxygen/hydrogen uptake and desorption during annealing. The slight increase in N_e suggests oxygen, hydrogen or H₂O desorption. However, decoupling these causes is challenging and requires dedicated measurements.^[27]

4.2. Tracking the Amorphous-to-Polycrystalline Transition in Zr-Doped In₂O₃ Films Grown by PLD and RF-Sputtering

To our knowledge, solid phase crystallization of In₂O₃-based TCOs, widely reported for sputtered films, has been less reported for films grown by PLD. Moreover, the crystal orientation and growth mechanism of these grains have not been described in detail. Here we use GI-XRD and in situ heating to determine the preferential orientation of the films and the evolution of the crystallization. **Figure 3** shows the XRD pattern of 100-nm as-deposited and annealed IZrO films. The absence of diffraction

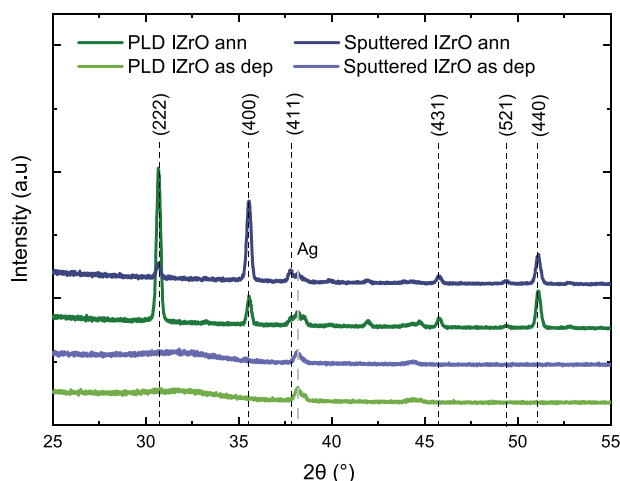


Figure 3. GI-XRD scan of the as-deposited and annealed IZrO films grown by PLD and RF-sputtering. In both cases, the as-deposited films are mostly amorphous with few crystalline seeds. The diffraction scans for the annealed samples indicate that the PLD and sputtered samples crystallize into In₂O₃ bixbyite cubic structure with distinct preferential orientations. The peak around 38.25° corresponds to silver contacts in the corners of the films required for preceding electrical characterization.

peaks for the as-deposited samples is indicative of mostly amorphous films. However, utilizing high-resolution GI-XRD (Figure S1, Supporting Information), we additionally observe the formation of two very low-intensity peaks close to the characteristic crystallographic planes of the In₂O₃ bixbyite cubic structure: (222) for the PLD-grown film and (400) plane for the sputtered film. Ex situ annealing of the samples at 200 °C leads to the formation of polycrystalline films with the initial preferential orientation of the nanocrystallites (Figure 3). GI-XRD scans during in situ heating in ambient atmosphere were furthermore performed at the temperature range from 125 to 225 °C to track the evolution of the crystallization and determine the amorphous-to-polycrystalline transition temperature. The measurements at each temperature (2 min 40 s in duration) was preceded by 2 min 30 s of stabilization time. The temperature step size was 5 °C, the heating rate was fixed at 25 °C min⁻¹. The contour plot comprising the XRD patterns measured at each temperature step is presented in **Figure 4**.

There are two main observations from Figure 4: one is related to the threshold temperature for crystallization, while the other one is related to the distinct intensities of the main peaks. The threshold temperature for full crystallization (measured at the highest peak intensity) for the PLD films is systematically lower: 145 °C versus 155 °C for the sputtered samples. This indicates higher activation energy for the crystallization process of the sputtered films. An annealing in the vicinity of the transition temperature (150 °C) reveals different crystallization rates

Table 1. Electrical properties of 100-nm-thick as-deposited and annealed at 200 °C IZrO films grown by RF-sputtering and PLD.

IZrO		N_e [10 ²⁰ cm ⁻³]	μ_{Hall} [cm ² V ⁻¹ s ⁻¹]	σ [S cm ⁻¹]	R_{sh} [Ω □ ⁻¹]
PLD	As-deposited	4.7	21	1470	68
	Annealed	5.5	71	4761	21
RF-sputtering	As-deposited	6.2	20	1920	52
	Annealed	3.2	77	3700	27

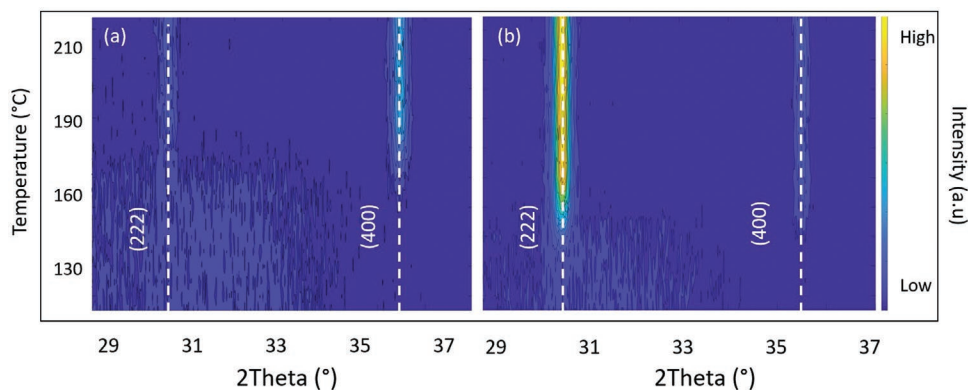


Figure 4. GI-XRD patterns measured during in-situ crystallization of IZrO films grown by RF-sputtering (a) and PLD (b). The y-axis indicates the temperature on the sample, the color bar corresponds to the intensity of the peaks.

for IZrO films fabricated by different deposition methods. Crystallization curves (derived from temperature-dependent XRD) were fitted using the Avrami equation for isothermal transition: $X_c = 1 - e^{-(Kt)^n}$, where X_c is the crystalline fraction, K is a temperature-dependent rate constant and n is an exponent that reflects the geometry of the transformation.^[28] The exponents n of the fitted curves were found to be ≈ 1.4 for sputtered and ≈ 2.2 for PLD-grown films (Figure S3, Supporting Information). The former reflects site-saturated growth, while the latter is explained by continuous nucleation growth model as suggested by Wang et al.^[29] We hypothesized that higher intensity of the main (222) peak in XRD scan for PLD IZrO film (Figure 4 and Figure S4, Supporting Information) and slightly bigger grains in the annealed state are due to the faster nucleation rate of these films. This was furthermore indicated by the larger value of Avrami exponent and higher density of nanocrystallites for PLD-grown films as shown by phase fraction determination analysis based on EBSD measurements (Table S1, Supporting Information).

Additionally, the slight differences in the crystalline transition might be related to the stoichiometry of the films. Wang et al.^[29] studied the crystallization of In_2O_3 in the presence and absence of water vapor and demonstrated the dependence of crystallization kinetics on the oxygen content of the film. As suggested by higher free carrier densities, sputtered films fabricated at lower process pressure and oxygen partial pressures than PLD films, may have higher amount of oxygen vacancies in the as-deposited state (Section 4.1). Other reports suggest a link between oxygen content and the preferential orientation of ITO, indicating that oxygen-deficient ITO present (200) preferential orientation, while stoichiometric films present (111) preferential orientation.^[30–32]

Nevertheless, there is no striking difference on the optoelectronic properties of the PLD and sputtered IZrO films (likely due to their polycrystalline nature) despite the distinct preferential orientation observed in all the experiments: (111) orientation in the case of PLD-grown films and (200) orientation in the case of sputtered films. This indicates that the optoelectronic properties of polycrystalline IZrO are independent of the preferential film orientation which, in its turn, is not a characteristic feature of the deposition method, but of the process parameters.

4.3. Electron Backscatter Diffraction

Electron backscatter diffraction (EBSD) was used to locally probe the crystallographic orientation of the IZrO films grown by PLD and by RF-sputtering. **Figure 5** shows the EBSD mapping on IZrO films as-deposited (left) and annealed at 200 °C in air (right). The figures demonstrate the presence of mainly amorphous phase at the as-deposited state (shown as black areas) with the presence of nanocrystallites with In_2O_3 phase. It is important to mention that pole figures represent crystal directions or plane normal of a material within the sample reference system. For cubic materials it is reduced to the standard triangle with (001), (111) and (010) orientations. Interestingly, the sputtered films show a higher density of nanocrystallites parallel to (001) and (010) orientations, while the nanocrystallites of the PLD-grown are mainly parallel to (111) direction. This preferential orientation of the peak is preserved after annealing, as observed by the higher density of (111) oriented grains (green areas) in the annealed PLD-grown films. In-depth analysis of the grain orientations at the X, Y, and Z axis is shown in Figure S5, Supporting Information. The EBSD results confirm the XRD data and, moreover, indicate that the preferential orientation of the nanocrystallites, formed during the deposition of the films, defines the final film orientation. Figure 5 and scanning electron microscope (SEM) images (Figure S6, Supporting Information) of annealed films indicate grain sizes of 200–300 nm in width, for films grown with both methods. PLD IZrO films seem to have slightly larger grains as also suggested by the higher intensity of the main peak in XRD measurements (Figure 3). This could be a consequence of the lower density of crystalline seeds in the PLD as-deposited IZrO, leading to slightly more space for the grains to grow as compared to the sputtered IZrO. This is in line with previous reports describing the effect of the density of crystalline seeds with the final grain size in IZrO.^[23] The correlation of density of crystalline seeds and final grain size was also reported for W- and Ce-doped In_2O_3 films deposited via sputtering and reactive plasma deposition (RPD).^[24] The formation of large and high crystal quality grains has a direct effect enhancing the electron mobility measured for both films and enable fabrication of thin films with comparable μ_e despite slight difference in crystal size.^[24,33] The preferential orientation of these films, in its turn,

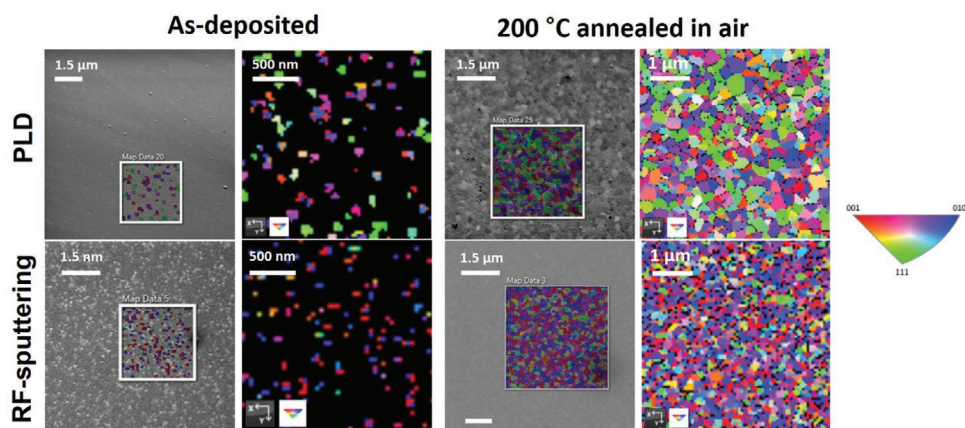


Figure 5. EBSD mapping on IZrO films as-deposited (left) and annealed at 200 °C in air (right) next to the corresponding SEM images. The black areas of the scans indicate amorphous material with the presence of nanocrystallites with In_2O_3 phase. The color code on the right of the figure indicate the crystallographic plane orientations.

appears to have minimal effect on the optoelectronic properties, as mentioned above.

4.4. Integration of PLD-Grown IZrO in Semi-Transparent Halide Perovskite Solar Cells (ST-PSC)

ST-PSC intended for both mechanically stacked four-terminal (4T) or monolithically integrated two-terminal (2T) tandem devices have two similar main bottlenecks to overcome related to transparent electrodes.^[34] One of them is loss of NIR transmittance due to parasitic absorption in the TCOs^[35] which is more pronounced for 4T case due to the increased number of transparent electrodes. The second one is integration of the TCO electrode by physical vapor deposition (PVD) methods on top of the sensitive halide perovskite and contact layers. The former is typically solved by utilizing TCOs with high mobility,^[36] while the latter is approached by inserting additional solution-processed metal oxide buffer layers^[37] or using “soft” landing methods on top of the perovskite layer.^[17,38] Our main objective is to show that PLD may serve as an alternative for damage-free deposition of TCOs in solar cells. To prove

the applicability of PLD for scalable fabrication of efficient ST-PSC for 4T devices, we implemented IZrO (as-deposited, mostly amorphous state) as the rear electrode and compared cell performance with reference opaque cells and semi-transparent cells with sputtered rear ITO. For a fair comparison of the electrical performance of the cells, the thicknesses of the IZrO (≈ 130 nm) and ITO (≈ 180 nm) were optimized to achieve $R_{\text{sh}} 50 \Omega \square^{-1}$ (both deposited at room temperature without post-treatment). A comparison of optoelectrical properties for typical TCO films employed in this study are provided in Figure S7 and Table S3, Supporting Information. The device stack and the different rear electrodes are shown in **Figure 6a**.

Figure 6b displays statistical distribution of power conversion efficiencies (PCE) for solar cells with different rear electrodes for both forward and reverse scan directions measured from the glass side. The star indicates the stabilized PCE that was obtained by tracking the output power for 300 s as shown in Figure 6c. No efficiency deterioration is observed for cells with either of the rear electrodes. PCE of the reference opaque cell is reaching 19.8% for the champion cell highlighting high quality of the halide absorber and relevant choice of the transport layers. Stabilized PCE of the ST-PSC cells with PLD-grown

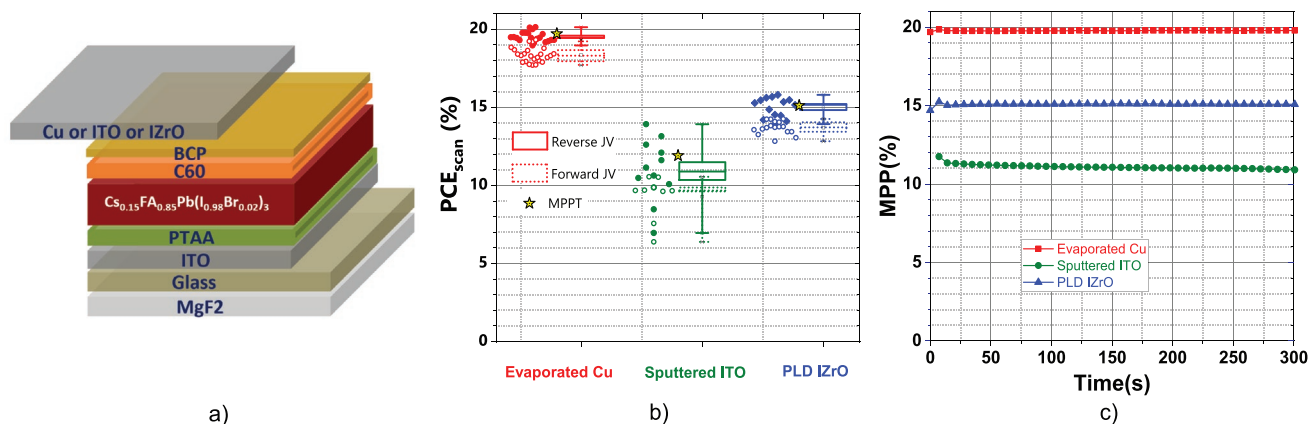


Figure 6. a) Cross-section of the perovskite solar cells (PSC) with different rear electrodes: evaporated Cu electrode for opaque cells or TCO grown by RF-sputtering or PLD in case of semi-transparent (ST) cells. b) Box plot of power conversion efficiencies measured for the fabricated solar cells with different electrodes for both forward and reverse scan directions. c) Maximum power point tracking of power conversion efficiency for the representative solar cells.

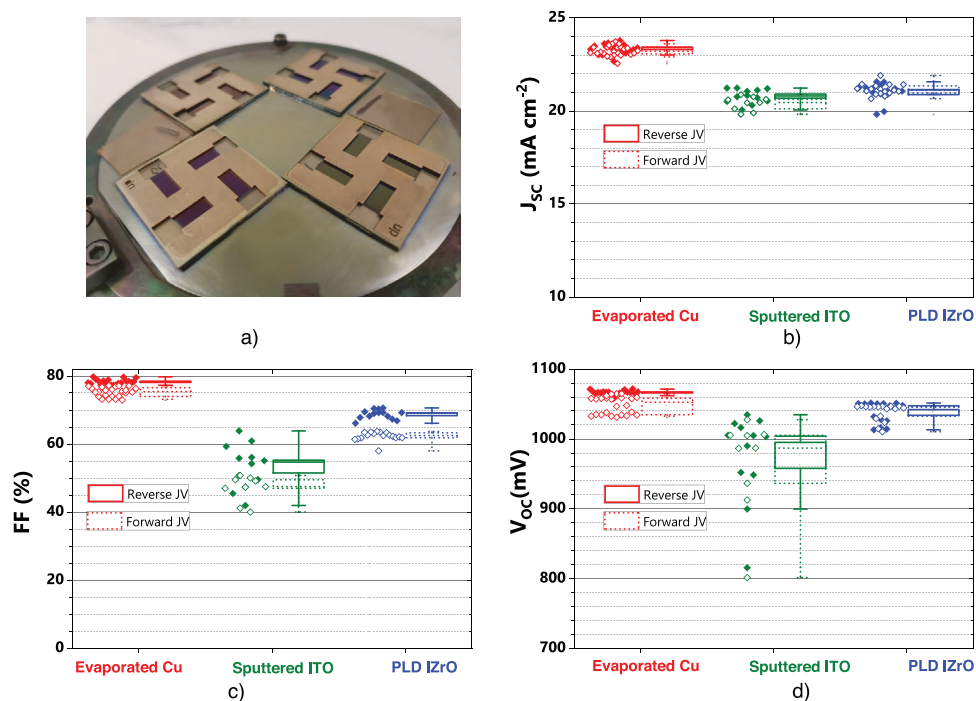


Figure 7. a) Photograph of 4 substrates (9 cm² area) with 4 cells each loaded on a 4-inch carrier wafer suitable for scalable solar cell fabrication. Reference glass samples included for TCO layer characterization. b) Short-circuit current density (J_{sc}), c) fill factor (FF), and d) open-circuit voltage (V_{oc}) extracted from current-voltage measurements of solar cells with varying rear TCO.

rear TCO is higher than of the counterparts with sputtered rear ITO (15.1% vs. 11.9%).

As seen in Figure 6b, cells with IZrO electrode demonstrate small variations on PCE. This proves batch-to-batch reproducibility in addition to uniformity of properties within a single deposition, as four substrates (9 cm² area), with 4 cells each, were simultaneously loaded on a 4-inch carrier wafer (Figure 7a). Further insights into the origins of the performance difference for ST-PSC could be extracted from the box plot of the solar cell parameters in Figure 7b–d: short-circuit current density (J_{sc}), open-circuit voltage (V_{oc}) and fill factor (FF). The J_{sc} of cells with either of the transparent electrodes demonstrate comparable values of around 21 mA cm⁻². This can be explained by the identical front ITO electrode leading to similar transparency in the spectral region of strong halide perovskite absorption (300–800 nm). However, the wider bandgap of IZrO as compared to ITO (Figure S7, Supporting Information) may lead to the increased photocurrent from UV photons if IZrO is placed also as front electrode in ST-PSC. Noteworthy, high transmittance in the 800–1200 nm region for both IZrO and ITO in the study is beneficial to increase J_{sc} in tandem devices with the bottom cell harvesting the NIR part of the spectrum.^[20,35,39]

In contrast to the J_{sc} , the FF, and V_{oc} differ significantly for ST-PSC with different rear TCOs. Cells with IZrO electrode demonstrate higher FF (68% vs. 55%) and V_{oc} (1050 mV vs. 1000 mV). Although there is some inhomogeneity in the cell parameters for ST-PSC with ITO and evaporated ETL in this experiment, we believe the results to be indicative of the performance deterioration for the cells with this specific sputtered ITO. First, it was previously shown^[39,40] that usage of 30-nm thick compact ZnO deposited by spatial atomic layer deposition

on top of ETL is critical to protect the cell during the described sputtering process of the top ITO layers. In this contribution we purposefully omit the additional layer to prove the advantage of PLD mitigating as a damage-free deposition process in contrast to sputtering. Second, the observed S-shaped J - V degradation (Figure S8, Supporting Information) for cells with ITO electrode reveals the sputter-induced damage of organic ETLs for the investigated devices. This potentially leads to the increased barrier height at ETL/TCO interface as suggested by Kanda et al.^[41] causing severe drop of FF and V_{oc} . This J - V degradation is not pronounced for the cells with PLD grown rear electrode. We link this to the higher deposition pressure during PLD in this study enabling thermalization of species arriving on the solar cell precursors.^[5,18] These process conditions could be achieved with other deposition methods including sputtering,^[17] however ignition at low power (a common requirement for low-damage sputter deposition) and high pressures may be problematic.^[42] Moreover, optoelectronic properties of TCO films and their density may be compromised at these process conditions.^[43,44] Although the demonstrated “soft” landing deposition is likely linked to the process conditions utilized specifically for the compared cases, PLD as a method is favoring larger deposition pressure range, since the energy source for material ablation (laser) is physically decoupled from the vacuum equipment. Additional experiments with sputtered films at high pressures (matching those of PLD) will help elucidate if other features from the methods influence the damage on the substrates. For example, more confined plasma during PLD (as compared to sputtering) may be beneficial for reducing the negative ion flux^[45,46] and thus mitigating the plasma damage.

Further studies for TCOs deposited by PLD are required to understand the relation between the process parameters and the properties of TCO/transport layer interface and, subsequently, solar cell performance. Nevertheless, obtained results clearly demonstrate that PLD holds a great potential for the scalable fabrication of high-efficiency solar cells enabling deposition on top of sensitive carrier transport layers as in case of perovskite solar cells.

5. Conclusion

In summary, we have developed a room-temperature pulsed laser deposition process to obtain Zr-doped In₂O₃ thin films with excellent optoelectronic properties on 4-inch wafers. High mobility (>60 cm² V⁻¹s⁻¹) and low absorptance (<10%) in 300–1200 nm spectral range after a mild annealing step at 200 °C in air makes PLD-grown electrodes appealing for silicon/perovskite four-terminal tandem solar cells. Higher deposition pressure during ablation (as compared to sputtering) enables damage-free TCO deposition on top of sensitive materials. High stabilized efficiency (15.1%) of semi-transparent perovskite solar cell with IZrO electrode produced by PLD verifies the great potential for this vacuum method for scalable fabrication of optoelectronic devices.

Supporting Information

Supporting Information is available from the Wiley Online Library or from the author.

Acknowledgements

The authors acknowledge Dr. Mark Smithers for SEM and EBSD measurements and Junke Wang for electron transport layer evaporation. The authors acknowledge financial support by the KAUST Center Partnership Fund Project OSR-2019-CPF-4106.4 and the SOLAR-ERA.NET, CUSTCO project. TNO is also acknowledged for financial support by the Early Research Program “Sustainability & Reliability for solar and other (opto-)electronic thin-film devices” (STAR). Y.S., P.A.R., and M.M.-M. thank Yorick Birkhölzer for help with X-ray diffraction measurements, Dr. Jaap Geessinck and Dr. Rik Groenen (TSST), Prof. Guus Rijnders and Prof. Gertjan Koster (University of Twente) for fruitful discussions on PLD growth.

Conflict of Interest

The authors declare no conflict of interest.

Keywords

magnetron sputtering, perovskite solar cells, pulsed laser deposition, transparent conducting oxides

Received: August 28, 2020
Revised: November 26, 2020
Published online:

- [1] D. Dijkkamp, T. Venkatesan, X. Wu, S. Shaheen, N. Jisrawi, Y. Min-Lee, W. McLean, M. Croft, *Appl. Phys. Lett.* **1987**, 51, 619.
- [2] H. Kim, a. C. Gilmore, A. Pique, J. Horwitz, H. Mattoussi, H. Murata, Z. Kafafi, D. Chrisey, *J. Appl. Phys.* **1999**, 86, 6451.
- [3] H. Kim, J. Horwitz, G. Kushto, S. Qadri, Z. Kafafi, D. Chrisey, *Appl. Phys. Lett.* **2001**, 78, 1050.
- [4] K. Matsubara, P. Fons, K. Iwata, A. Yamada, K. Sakurai, H. Tampo, S. Niki, *Thin Solid Films* **2003**, 431, 369.
- [5] S. Schubert, F. Schmidt, H. von Wenckstern, M. Grundmann, K. Leo, L. Müller-Meskamp, *Adv. Funct. Mater.* **2015**, 25, 4321.
- [6] J. H. Park, J. Seo, S. Park, S. S. Shin, Y. C. Kim, N. J. Jeon, H.-W. Shin, T. K. Ahn, J. H. Noh, S. C. Yoon, C. S. Hwang, S. I. Seok, *Adv. Mater.* **2015**, 27, 4013.
- [7] Y. H. Jo, B. C. Mohanty, Y. S. Cho, *Sol. Energy* **2010**, 84, 2213.
- [8] A. Cazzaniga, A. Crovetto, C. Yan, K. Sun, X. Hao, J. R. Estelrich, S. Canulescu, E. Stamate, N. Pryds, O. Hansen, *Solar Energy Mater. Solar Cells* **2017**, 166, 91.
- [9] E. T. Barraza, W. A. Dunlap-Shohl, D. B. Mitzi, A. D. Stiff-Roberts, *J. Electron. Mater.* **2018**, 47, 917.
- [10] V. M. Kiyek, Y. A. Birkhölzer, Y. Smirnov, M. Ledinsky, Z. Remes, J. Momand, B. J. Kooi, G. Koster, G. Rijnders, M. Morales-Masis, *Adv. Mater. Interfaces* **2020**, 7, 2000162.
- [11] J. A. Greer, *J. Phys. D: Appl. Phys.* **2013**, 47, 034005.
- [12] D. H. Blank, M. Dekkers, G. Rijnders, *J. Phys. D: Appl. Phys.* **2013**, 47, 034006.
- [13] S. Lee, V. Petrykin, A. Molodyk, S. Samoilonkov, A. Kaul, A. Vavilov, V. Vysotsky, S. Fetisov, *Supercond. Sci. Technol.* **2014**, 27, 044022.
- [14] J. Schou, *Appl. Surf. Sci.* **2009**, 255, 5191.
- [15] P. Willmott, *Prog. Surf. Sci.* **2004**, 76, 163.
- [16] G. J. Rijnders, G. Koster, D. H. Blank, H. Rogalla, *Appl. Phys. Lett.* **1997**, 70, 1888.
- [17] R. A. Jagt, T. N. Huq, S. A. Hill, M. Thway, T. Liu, M. Napari, B. Roose, K. Gałkowski, W. Li, S. F. Lin, S. D. Stranks, J. L. MacManus-Driscoll, R. L. Z. Hoyer, *ACS Energy Lett.* **2020**, 5, 2456.
- [18] J. B. Franklin, L. R. Fleet, C. H. Burgess, M. A. McLachlan, *Thin Solid Films* **2014**, 570, 129.
- [19] M. Morales-Masis, E. Rucavado, R. Monnard, L. Barraud, J. Holovsky, M. Despeisse, M. Boccard, C. Ballif, *IEEE J. Photovoltaics* **2018**, 8, 1202.
- [20] E. Aydin, M. De Bastiani, X. Yang, M. Sajjad, F. Aljamaan, Y. Smirnov, M. N. Hedhili, W. Liu, T. G. Allen, L. Xu, E. Van Kerschaver, M. Morales-Masis, U. Schwingenschlgl, S. De Wolf, *Adv. Funct. Mater.* **2019**, 29, 1901741.
- [21] D. Głowienka, F. Di Giacomo, M. Najafi, I. Dogan, A. Mameli, F. J. Colberts, J. Szymkowski, Y. Galagan, *ACS Appl. Energy Mater.* **2020**, 3, 8285.
- [22] H. F. Wardenga, M. V. Frischbier, M. Morales-Masis, A. Klein, *Materials* **2015**, 8, 561.
- [23] E. Rucavado, F. Landucci, M. Döbeli, Q. Jeangros, M. Boccard, A. Hessler-Wyser, C. Ballif, M. Morales-Masis, *Phys. Rev. Mater.* **2019**, 3, 084608.
- [24] T. Koida, Y. Ueno, H. Shibata, *Phys. Status Solidi A* **2018**, 215, 1700506.
- [25] M. P. Taylor, D. W. Readey, M. F. van Hest, C. W. Teplin, J. L. Alleman, M. S. Dabney, L. M. Gedvilas, B. M. Keyes, B. To, J. D. Perkins, D. S. Ginley, *Adv. Funct. Mater.* **2008**, 18, 3169.
- [26] J. De Wit, G. Van Unen, M. Lahey, *J. Phys. Chem. Solids* **1977**, 38, 819.
- [27] T. Koida, M. Kondo, K. Tsutsumi, A. Sakaguchi, M. Suzuki, H. Fujiwara, *J. Appl. Phys.* **2010**, 107, 033514.
- [28] M. Avrami, *J. Chem. Phys.* **1939**, 7, 1103.
- [29] M. Wang, Y. Sawada, H. Lei, Y. Seki, Y. Hoshi, T. Uchida, T. Konya, A. Kishi, *Thin Solid Films* **2010**, 518, 2992.
- [30] E. Terzini, P. Thilakan, C. Minarini, *Mater. Sci. Eng., B* **2000**, 77, 110.
- [31] M. Wang, Y. Onai, Y. Hoshi, H. Lei, T. Kondo, T. Uchida, S. Singkarat, T. Kamwanna, S. Dangtip, S. Aukkaravittayapun, *Thin Solid Films* **2008**, 516, 5809.

- [32] D. Kim, Y. Han, J.-S. Cho, S.-K. Koh, *Thin Solid Films* **2000**, 377, 81.
- [33] Y. Jiang, T. Feurer, R. Carron, G. Torres-Sevilla, T. Moser, S. Pisoni, R. Erni, M. D. Rossell, M. Ochoa, R. Hertwig, *ACS Nano* **2020**, 14, 7502.
- [34] J. Werner, B. Niesen, C. Ballif, *Adv. Mater. Interfaces* **2018**, 5, 1700731.
- [35] B. Chen, S.-W. Baek, Y. Hou, E. Aydin, M. De Bastiani, B. Scheffel, A. Proppe, Z. Huang, M. Wei, Y.-K. Wang, E.-H. Jung, T. G. Allen, E. Van Kerschaver, F. P. Garcde Arquer, M. I. Saidaminov, S. Hoogland, S. De Wolf, E. H. Sargent, *Nat. Commun.* **2020**, 11, 1257.
- [36] M. Morales-Masis, S. De Wolf, R. Woods-Robinson, J. W. Ager, C. Ballif, *Adv. Electron. Mater.* **2017**, 3, 1600529.
- [37] K. A. Bush, C. D. Bailie, Y. Chen, A. R. Bowering, W. Wang, W. Ma, T. Leijtens, F. Moghadam, M. D. McGehee, *Adv. Mater.* **2016**, 28, 3937.
- [38] B. Shi, L. Duan, Y. Zhao, J. Luo, X. Zhang, *Adv. Mater.* **2020**, 32, 1806474.
- [39] D. Zhang, M. Najafi, V. Zardetto, M. Dörenkämper, X. Zhou, S. Veenstra, L. Geerligs, T. Aernouts, R. Andriessen, *Solar Energy Mater. Solar Cells* **2018**, 188, 1.
- [40] M. Najafi, V. Zardetto, D. Zhang, D. Koushik, M. S. Dörenkämper, M. Creatore, R. Andriessen, P. Poodt, S. Veenstra, *Sol. RRL* **2018**, 2, 1800147.
- [41] H. Kanda, A. Uzum, A. K. Baranwal, T. N. Peiris, T. Umeyama, H. Imahori, H. Segawa, T. Miyasaka, S. Ito, *J. Phys. Chem. C* **2016**, 120, 28441.
- [42] A. J. Bett, K. M. Winkler, M. Bivour, L. Cojocar, O. S. Kabakli, P. S. Schulze, G. Siefer, L. Tutsch, M. Hermle, S. W. Glunz, *ACS Appl. Mater. Interfaces* **2019**, 11, 45796.
- [43] C. Vasant Kumar, A. Mansingh, *J. Appl. Phys.* **1989**, 65, 1270.
- [44] L. Tutsch, M. Bivour, W. Wolke, M. Hermle, J. Rentsch, in *Proceedings of the 33rd European PV Solar Energy Conference*, Amsterdam, **2017**, pp. 720–724.
- [45] T. Jäger, Y. E. Romanyuk, A. N. Tiwari, A. Anders, *J. Appl. Phys.* **2014**, 116, 033301.
- [46] A. Illiberi, P. Kudlacek, A. Smets, M. Creatore, M. Van De Sanden, *Appl. Phys. Lett.* **2011**, 98, 242115.